Electronic Supplementary Material (ESI) for Nanoscale.

Supplementary Information

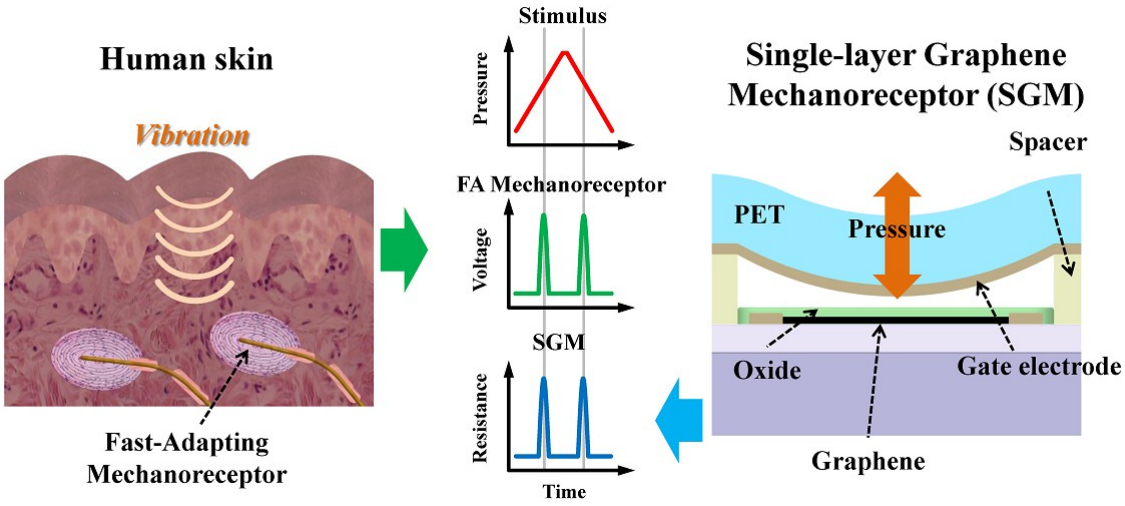

Supplementary Figure S1. Bio-mimicry of a fast-adapting receptor. Fast-adapting type mechanoreceptors generate action potentials only when there are pressure variations. The graphene mechanoreceptor mimics such behavior by having a flexible membrane gate utilizing electrical field effect on channel transport. Dirac point is adjusted so that the resistance becomes maximized at a specific gap between the gate and graphene. The resistance spikes are generated once in the pressure application and again in the pressure release.

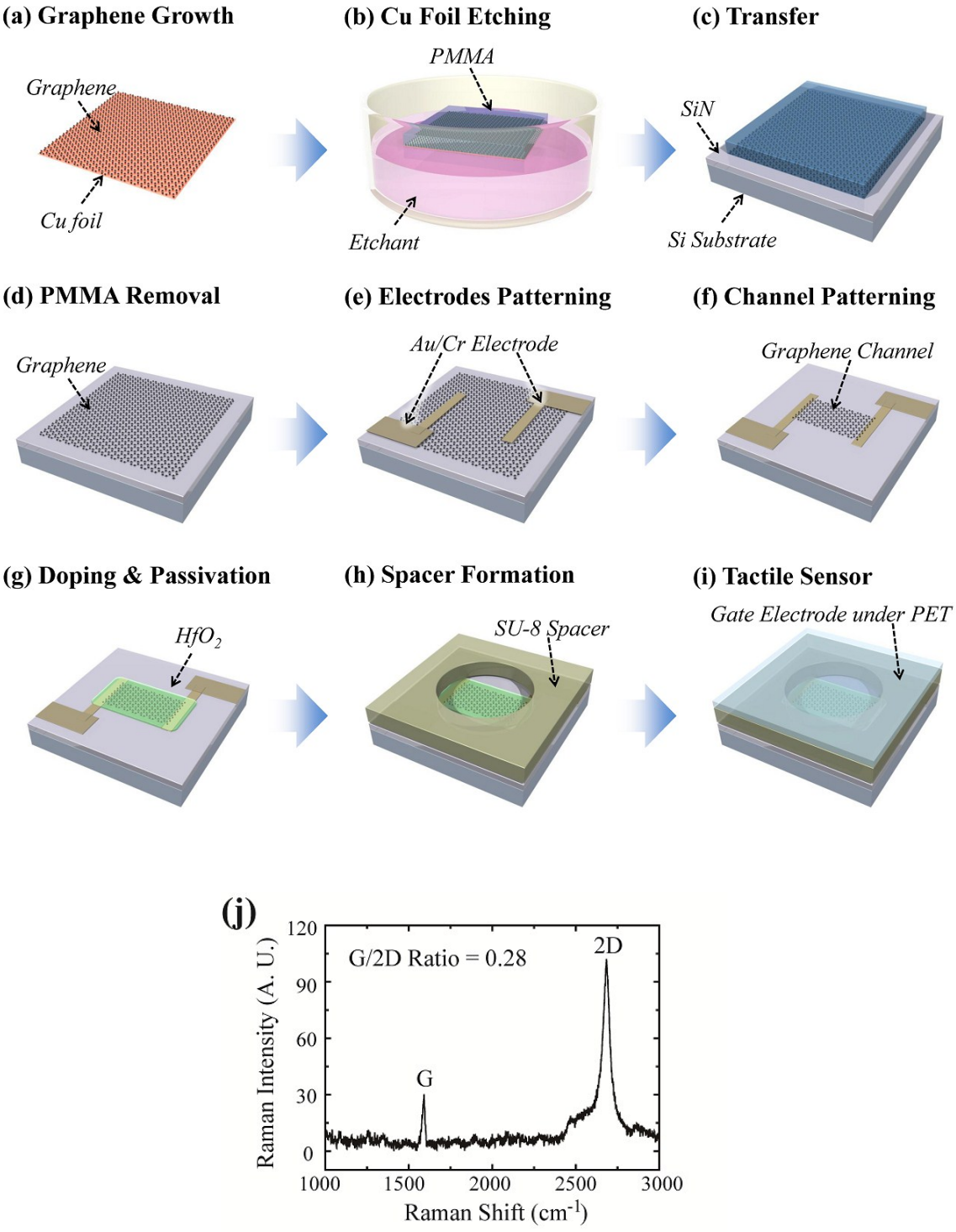

Supplementary Figure S2 Process flow for graphene pressure sensor fabrication. See the following text for details.

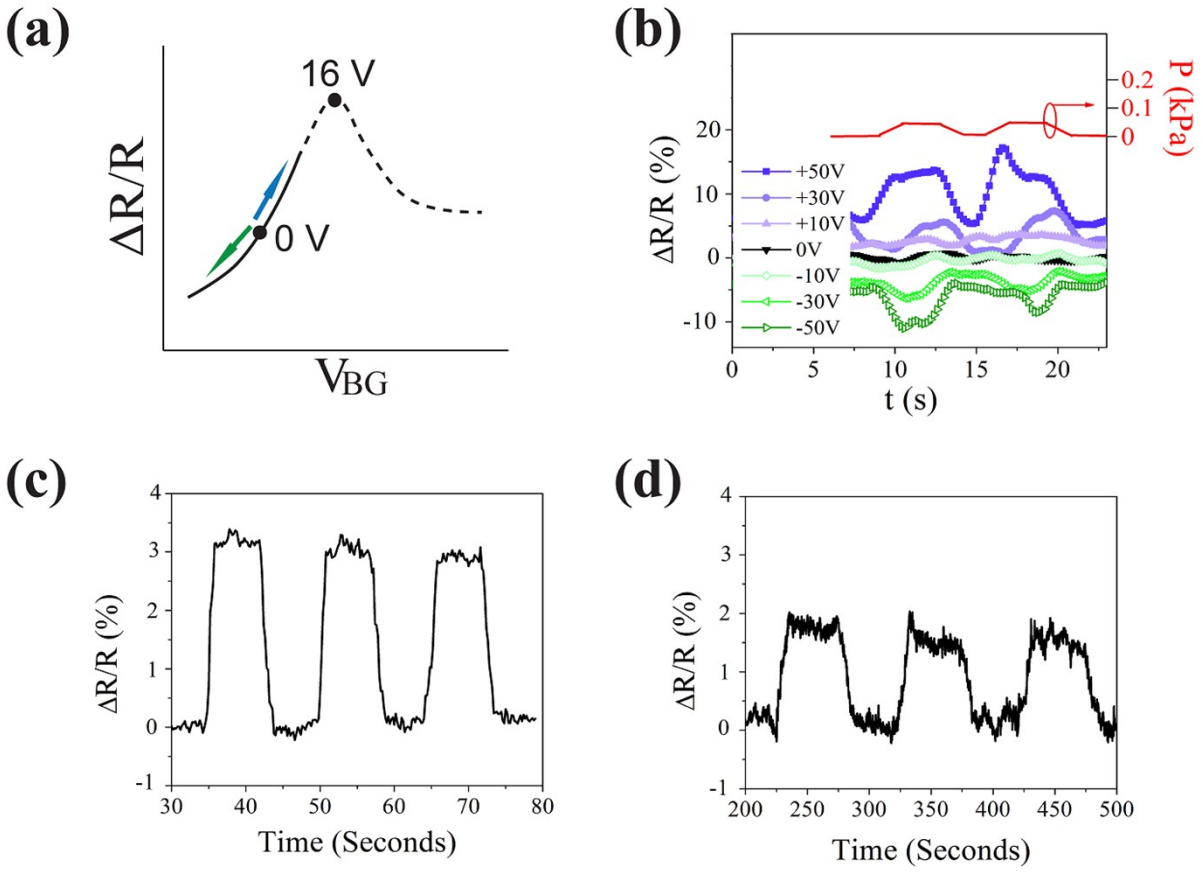

Supplementary Figure S3 Denting tests well away from Dirac points in two different denting speeds. (a) Expected schematic change of resistance by the membrane gate's approach (blue arrow) and retraction (green arrow) based on a transconductance curve, if Fermi levels sweep range is away from Dirac point. (b) Measured resistance traces without crossing Dirac point in various gate potentials, from -50 V to 50 V in 10 V steps. The movement of effector was programmed to follow a pressure profile shown in red. (c) The effector tip was pressurized and depressurized in three cycles, and the effector speed was 10 μm/s. and (d) was 1.67 μm/s. The gate voltage was 20 Volts for both tests.

Pressurizing tests well away from Dirac points in two different pressurizing speeds.

To verify the field-effect of the deflecting flexible gate on graphene transport, we performed transducing tests at the graphene's hole transport regime. Figure S3(a) shows how the graphene resistance would change depending on the flexible gate movement at positive and negative gate potentials. When pressure is applied and the gate approaches the channel with positive voltage, it emulates the effect of the backgate being swept in the positive direction (blue arrow) starting from 0 V, as shown in figure 2(c). Here, the field strength of the approaching gate is not strong enough to have the Fermi level exceed the Dirac voltage. With a negative flexible gate potential, the field will resemble a negative backgate sweep resulting in the graphene resistance being reduced (green arrow). Since the Dirac point is kept outside of the Fermi level sweep range, the graphene resistance will show a graded response depending on the polarity and magnitude of the gate potential. Figure S3(b) shows the time evolution of the graphene resistance variation depending on applied cyclic pressures for different V_{FG} values, varied from -50 V to 50 V in 10 V steps. The results show that the higher the gate potential's absolute value, the more effect it had on the graphene resistance for the same gate deflection height. When the effector speed was varied, the resistance slope followed the speed (Figure S3(c) & (d)). These observations indicate that the change in graphene resistance came from the change in gate field strength which was due to the pressure induced deflection of the flexible gate and not from any short between the gate and the contacts or the graphene channel.

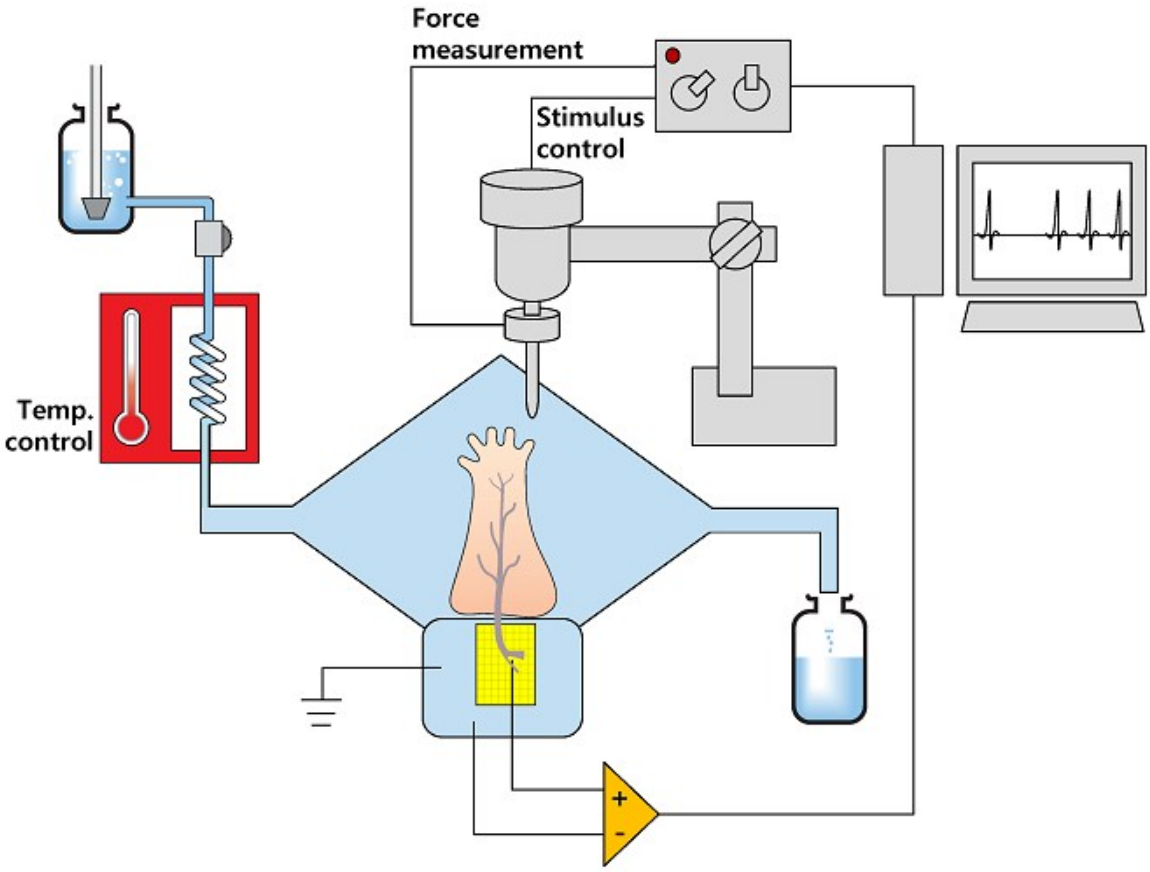

Supplementary Figure S4. Schematic of the *ex vivo* skin–nerve preparation. The skin from hindlimb of a mouse was mounted on a perfusion chamber. Attached saphenous nerve was resting on a mirror in the adjacent recording chamber. Chamber was perfused with synthetic interstitial fluid (SIF) being gassed with carbogen and maintained at 30°C. Mechanical stimulator and load cell mounted on the cantilever arm was connected to a controller. Mechanical probe tip was attached to the bottom of a load cell. Amplified action potentials and applied stimulus data were collected by PC.

Surgical procedure and ex-vivo recording

All animal experiments were performed according to the guidelines of the Animal and Plant Quarantine Agency of Korea for the care and use of laboratory animals, and the study was approved by the Institutional Animal Care and Use Committee of Hanyang University (HY-IACUC-15-0113).

An animal was sacrificed by asphyxiation with CO_2 and the hair in the posterior leg was shaved with an electric razor and plantar surface of the foot was fixed on a linen. The saphenous nerve was after a circular incision of the skin around the knee joint. Then a circular cut at the lateral edge of the foot keeping the hairy skin on the phalanges. And a bisection of the skin on the back of the calf with a straight incision to the direction of Achilles tendon was followed. Separating the hairy skin subcutaneously proximal from the toes to the femoral nerve removing adhesions with a pair of spring scissors. Separating the skin with the saphenous nerve attached.

A delrin organ bath chamber was perfused with warm synthetic interstitial fluid (sodium chloride 107.8 mM, potassium chloride 3.5 mM, magnesium sulphate, heptahydrate 0.69 mM, sodium bicarbonate 26.2 mM, sodium phosphate monobasic, dihydrate 1.67 mM, gluconic acid sodium salt 9.64 mM, glucose 5.55 mM, sucrose 7.6 mM, and CaCl2 1.53mM gassed with mixture of 95% O_2 and 5% CO_2; carbogen) that was made fresh before each experiment. Skin-nerve preparation was mounted dermis side up and pinned on the chamber where the bottom of the bath was coated with silicone elastomer. Then the nerve was dragged into the adjacent smaller recording chamber via a hole. The nerve was desheathed and whole fibers were teased into thin strands using fine forceps so that few fibers are isolated for high signal-to-noise ratio. After attaching a strand on the electrode, a light pressure with a blunt-tipped rod was applied to confirm a FA type response. This was repeated until a FA receptor with clear waveform was found. When a single FA was identified, its mechanical threshold was

measured first. A mechanical stimulator was placed to enable precise application of pressure on the connected receptive field. Then a ramp stimulus that designed to reach the range of 1 to 2 fold of the threshold (70~80 kPA, tip diameter of 1 mm) was applied. The stimulus continues about 1second after reaching peak pressure, and returns to zero with same slew rate with increasing.

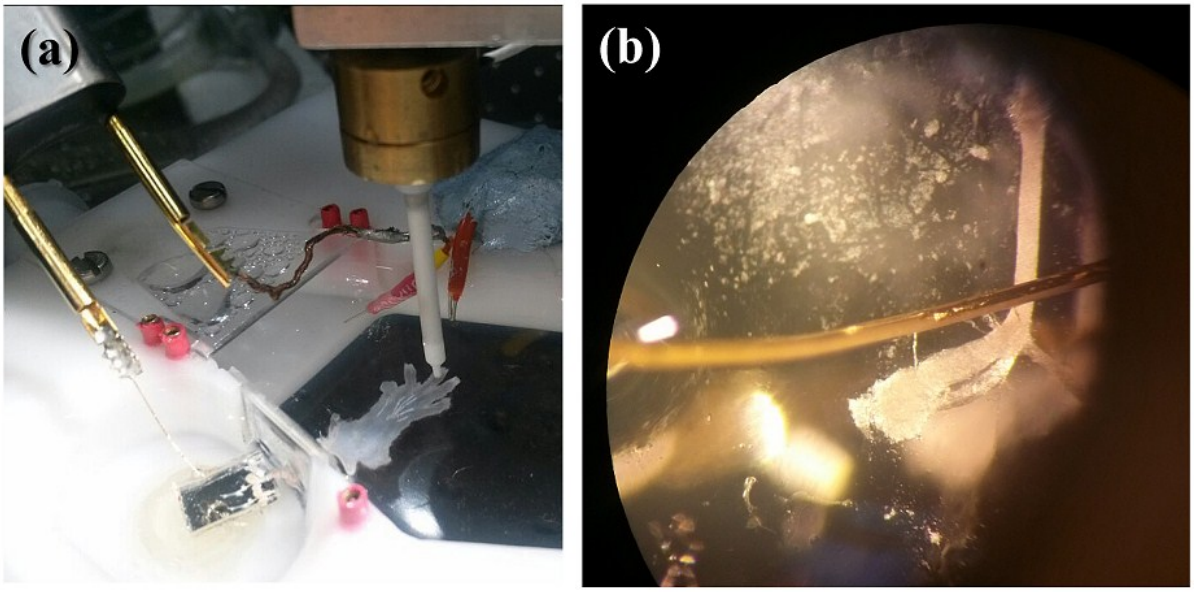

Supplementary Figure S5. Images of the *ex vivo* skin–nerve stimulation measurement. (a) Image of skin–nerve preparation mounted in the chamber. Mechanical probe tip was placed above the receptive field. (b) The cut end of the nerve was placed on the mirror. Optical microscope was provided to desheath the perineurium on the nerve, and tease into thinner bundle. The bundle was suspended on the pure gold wire recording electrode for recording.

Setup for ex-vivo recording

On the anti-vibration table, the chamber was placed in the middle with a binocular microscope (Olympus Co., Tokyo, Japan). Light guides from the fiber-optic light source (Dolan-Jenner, Dayton, USA) were adjusted to brighten the chamber. Pure gold wire electrodes were plugged on cathode and anode of the headstage of a differential amplifier (DP 311, Warner instruments, Hamden, USA). Action potential and the stimulation values were transmitted in data acquisition board (DAP5200a, Microstar laboratories Inc., Bellevue, USA) and sampled at 10 kHz in PC also being monitored via an oscilloscope. Using the window discrimination feature of the software (Dapsys 8; Brian Turnquist, Bethel University, St. Paul, USA), only the action potentials with same waveform of each single fiber were selectively recorded. The action potential data in this study was obtained by extracellular single unit recording. The gold wire electrode was place outside of the cellular membrane and the signals were much smaller than those in the intracellular recording methods, which otherwise would be from -70 mV to +50 mV. We took the extracellular method to ensure the least damage to the neuron. More detailed information on this method is included in box1 in a report[2].

Under the metal shaft of the mechanical stimulator, a cylindrical probe tip (1mm diameter) was attached. The movement of stimulator was driven by a solenoid with sinusoidal half-wave as command signal. Pressure under the tip was measured using a load cell (strain gauge) fixed to the distal metal shaft of the mechanical stimulator. Output voltage from the load cell was amplified (GSV-11L,ME-Messsysteme,Henningsdorf, Germany) and stored in PC[3].

During the ex-vivo recording, SIF was contained in a bottle placed higher than the chamber. The outlet was connected to a Liebig condenser heated by a pump-driven heating circulator. The heated SIF was continuously supplied to the chamber at a speed maintaining

the temperature 30-32°C using an i.v. extension set. Thermocouple was attached to the chamber to measure the temperature of the fluid. All the electrical devices except the light source was placed in a tower rack outside the table. Copper blocks were connected to common ground preventing excessive noise as a reservoir of current[2].

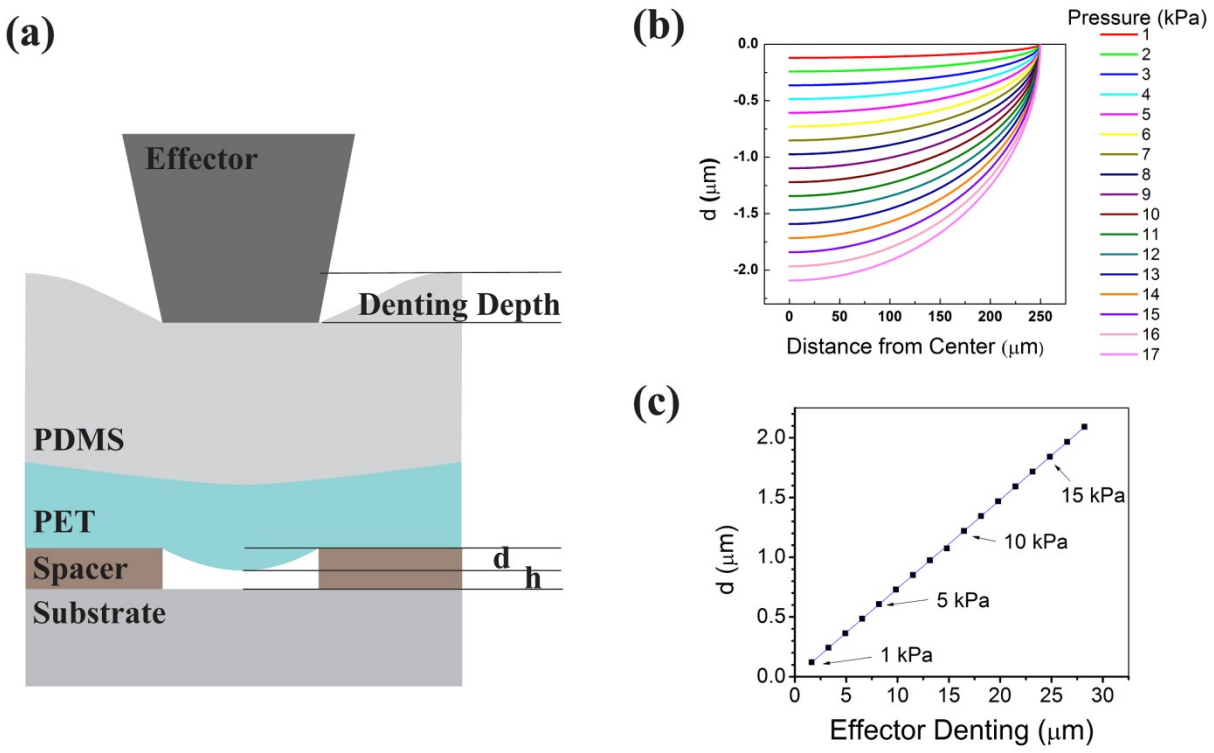

Supplementary Figure S6 Simulation of the gap between floating gate and graphene. (a) Schematically drawn deformation of PDMS slab by the effector's pressure. (b) Simulated profile of the bottom surface of the PDMS depending on the effector tip's pressure, spanning from center to edge of the spacer hole. (c) Simulated deformation, d, by effector's denting depth.

Simulation Method.

The conductance of graphene G, is written as[4],

$$G = \frac{2q^2}{h}\lambda(E_F)\frac{2E_F}{\pi\hbar v_F}, \text{ (S1)}$$

where q is the unit charge, $\hbar$ is Plank constant, E_F is Fermi level, v_F is the Fermi velocity,

and λ is the mean free path at Fermi energy. The mean free path was found to be proportional to Fermi level by the charged impurity scattering[5]. Thus, the resistance, R is proportional to the inverse square of E_f.

$$R \propto E_F^{-2} \quad \text{(S2)}$$

From figure 3(c), we know the relationship between backgate voltage V_{BG} and resistance. We can convert the voltage into Fermi level E_F. First, the amount of charge carriers induced by the capacitance effect between the backgate and the graphene channel is;

$$qn = \frac{C}{A} V_{BG}, \quad \text{(S3)}$$

where q is the unit charge, n is the number of charge carrier, C is the capacitance, and A is the area of the capacitor. Here we used a simple parallel capacitor model for 90 nm silicon nitride film. ($C/A \approx 3\times10^{-2}\mu F/cm^2$) We will ignore quantum capacitance of graphene because quantum capacitance is much larger than geometrical capacitance[6]. Then we have Fermi energy as[7],

$$E_F = \hbar v_F \sqrt{\pi n} = \hbar v_F \sqrt{\pi} \sqrt{\left(\frac{C}{A}\right)\left(\frac{V_{BG}}{q}\right)} \quad \text{(S4)}$$

However, there are impurities, n_0 in graphene and thus Dirac voltage shift V_0.

$$E_F = \hbar v_F \sqrt{\pi(n - n_0)} = \hbar v_F \sqrt{\frac{\pi}{q}} \sqrt{\left(\frac{C}{A}\right)(V_{BG} - V_0)} \cong 0.3\sqrt{V}\,(eV), \quad \text{(S5)}$$

where $V = V_{BG} - V_0$. We used this equation to obtain resistance versus Fermi energy equation. We first fit the V_{BG} vs. R data in figure 3(c) into a phenomenological 8th order polynomial equation,

$$R(V_{BG}) = 1486 + 154V_{BG} + 11.7V_{BG}^2 - 0.727V_{BG}^3 - 0.0256V_{BG}^4 + 2.33\times10^{-3}V_{BG}^5 - 5.67\times10^{-5}V_{BG}^6 + 5.96\times10^{-6}V_{BG}^7 - 2.34\times10^{-9}V_{BG}^8,$$

(S6)

because this result agrees well with the measurement. (S5) can be converted in terms of V_{BG} depending on polarity of E_F. If $V_{BG} > V_0 (E_F > 0)$, we have $V_{BG} = E_F^2/0.09 + V_0$, and if $V_{BG} < V_0 (E_F < 0)$, $V_{BG} = V_0 - E_F^2/0.09$. Then we can have equation, $R = R(E_F)$ relating resistance and Fermi level using (S6).

The charge carriers by the membrane gate can be obtained by the same logic.

$$E_F = \pm\hbar v_F \sqrt{\pi|m - n_0|} = \pm\hbar v_F \sqrt{\frac{\pi}{q}} \sqrt{\left|\frac{C_{Air}V_{FG}}{A} - \frac{CV_0}{A}\right|} = \pm\hbar v_F \sqrt{\frac{\pi}{q}} \sqrt{\left|\frac{\varepsilon_0\varepsilon_{Air}V_{FG}}{h} - \frac{\varepsilon_0\varepsilon_{SiN}V_0}{90nm}\right|} \quad \text{(S7)}$$

, in which m is the number of charge carriers induced by the membrane gate, and h is the distance between the membrane gate and graphene. Thus, we have Fermi level control by the distance, h.

The approach of the membrane gate, h, was simulated by FEMLAB (Comsol). We assumed 3 mm thickness of PDMS was pressed by an effector tip, which has same diameter with the space hole diameter (500μm). (Supplementary Figure 3) The roles of the PET film were transfer of downward movement of the PDMS and prevention of PDMS stick on the device. Other than those, the PET film had no other effect, so we removed it from the simulation. Here an effector tip was assumed to give an amount of pressure at the top surface of the PDMS. When a known amount of pressure was applied on the top surface of the PDMS, PDMS layer was pressed and squeezed to reduce the downward movement of the effector.

Table S1 shows the simulation results; the effector's pressure, denting depth of the PDMS at the PDMS top surface, and the movement of bottom PDMS surface near graphene channel, d.

As can be seen in the bottom PDMS movement column, fine movement of about 120 nm per 1.6 microns denting was possible due to the PDMS cushioning. Supplementary Figure 3(c) shows that the denting depth and *d* are linear in the simulated range;

$$d(\mu m) = -0.00219 + (0.074 \times d_{Eff}(\mu m)) \quad \text{(S8)}$$

where d_{Eff} is the denting depth of the effector.

The movement of the effector tip was controlled by a step motor with a constant velocity, 1.67 μm/second, we could set $d_{Eff} = v_{Eff} \times T$, where v_{Eff} = 1.67 μm/second, and T is time in seconds. Then the distance, *h*, is,

$$h = 2\mu m - d = 2\mu m - (-0.00219 + 0.074 \times v_{Eff} \times T) \quad \text{(S9)}$$

Equation (S8) and (S9) was plugged into equations (S7) to obtain the result in figure 4(f).

The simulated pressure of the effector in the Table 1 is much larger than measurements in figure 4(f), but there are two factors for consideration. First, the measured pressure is the pressure applied on the air piston, whose diameter is about 10 times larger than the tip of the effector. Thus the actual pressure applied on the top PDMS surface is 10 times larger than measurements in figure 3. Second, the simulation does not consider the sliding between layers; between PET and SU-8 spacer, and between PET and PDMS layer. In the actual denting tests, PET and PDMS layers are not laminated on SU-8 and they are free to slide laterally. Such sliding could possibly reduce pressure measurements.

Supplementary Table 1 Simulation parameters.

Pressure (kPa)	Denting Depth d_{Eff} (μm)	PDMS bottom surface movement d (μm)
1	1.63	0.12
2	3.26	0.24
3	4.90	0.36
4	6.55	0.48
5	8.19	0.60
6	9.84	0.72
7	11.4	0.85
8	13.1	0.97
9	14.8	1.07
10	16.4	1.22
11	18.1	1.34
12	19.8	1.46
13	21.4	1.59
14	23.1	1.71
15	24.8	1.84
16	26.5	1.96
17	28.2	2.09

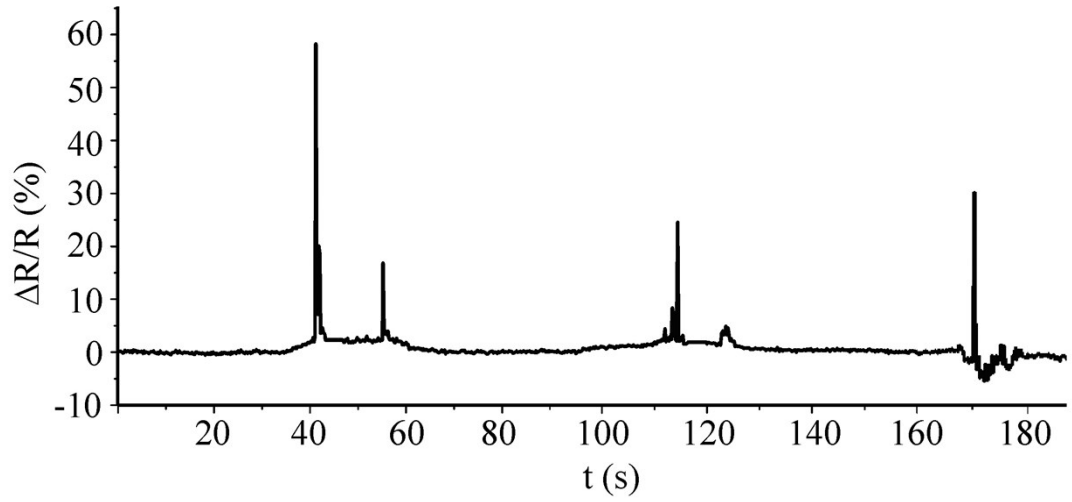

Supplementary Figure S7 Repeated pulse generations by 30V Resistance measurement under second (center) and third (right) pressurization cycles after the first cycle (left) shown in the figure 3(b).

Supplementary References

1. Chun, S., Kim, Y., Jin, H., Choi, E., Lee, S.-B., Park, W. A graphene force sensor with pressure-amplifying structure. *Carbon* **78** 601 (2014).

2. Zimmermann, K., A. Hein, U. Hager, J. S. Kaczmarek, B. P. Turnquist, D. E. Clapham and P. W. Reeh. Phenotyping sensory nerve endings in vitro in the mouse. *Nat. Protoc.* **4** 174 (2009).

3. De Col, R., K. Messlinger and R. W. Carr. Repetitive activity slows axonal conduction velocity and concomitantly increases mechanical activation threshold in single axons of the rat cranial dura. *J. Physiol* **590** 725 (2012).

4. Berdebes, D., Low, T., Lundstrom, M. *Low bias transport in graphene: An introduction*. Lecture notes in *NCN@Purdue summer school: Electronics from the bottom up*. (West Lafayette, IN, U.S.A., July 20-24, 2009).

5. Peres, N. M. R., Lopes dos Santos, J. M. B. & Stauber, T. Phenomenological study of the electronic transport coefficients of graphene. *Physical Review B* **76** 073412 (2007).

6. Xia, J., Chen, F., Li, J. & Tao, N. Measurement of the quantum capacitance of graphene. *Nature Nanotechnology* **4** 505 (2009).

7. Das Sarma, S., Adam, S., Hwnag, E. H. & Rossi, E. Electronic transport in two-dimensional graphene. *Rev. Mod. Phys.* **83** 407 (2011).